Hot-Carrier Cooling in High-Quality Graphene is Intrinsically Limited by Optical Phonons

Eva A. A. Pogna,[†,‡] Xiaoyu Jia,[¶] Alessandro Principi,[§] Alexander Block,[‖] Luca Banszerus,[⊥] Jincan Zhang,[#,@] Xiaoting Liu,[#,@] Thibault Sohier,[△] Stiven Forti,[▽] Karuppasamy Soundarapandian,[††] Bernat Terrés,[††] Jake D. Mehew,[‖] Chiara Trovatello,[‡] Camilla Coletti,[▽,‡‡] Frank H.L. Koppens,[††,¶¶] Mischa Bonn,[¶] Hai I. Wang,[¶] Niek van Hulst,[††,¶¶] Matthieu J. Verstraete,[△] Hailin Peng,[#,@] Zhongfan Liu,[#,@] Christoph Stampfer,[⊥] Giulio Cerullo,[‡] and Klaas-Jan Tielrooij*[,‖]

†*NEST, Istituto Nanoscienze-CNR and Scuola Normale Superiore, 56127 Pisa, Italy*

‡*Department of Physics, Politecnico di Milano, 20133 Milan, Italy*

¶*Max-Planck-Institut für Polymerforschung, 55128 Mainz, Germany*

§*School of Physics and Astronomy, University of Manchester, M13 9PL, Manchester, UK*

‖*Catalan Institute of Nanoscience and Nanotechnology (ICN2), BIST & CSIC, Campus UAB, Bellaterra (Barcelona), 08193, Spain*

⊥*JARA-FIT and 2nd Institute of Physics, RWTH Aachen University, 52074 Aachen, Germany, EU*

#*Center for Nanochemistry, College of Chemistry and Molecular Engineering, Academy for Advanced Interdisciplinary Studies, Peking University, Beijing 100871, China*

@*Beijing Graphene Institute, Beijing 100095, P. R. China*

△*NanoMat/Q-Mat/CESAM, Université de Liège (B5), B-4000 Liège, Belgium*

▽*Center for Nanotechnology Innovation IIT@NEST, Piazza San Silvestro 12, 56127 Pisa, Italy*

††*ICFO - Institut de Ciències Fotòniques, BIST, Castelldefels (Barcelona) 08860, Spain*

‡‡*Graphene Labs, Via Morego 30, 16163 Genova, Italy*

¶¶*ICREA - Institució Catalana de Reçerca i Estudis Avancats, 08010 Barcelona, Spain*

E-mail: klaas.tielrooij@icn2.cat

Supporting Information

1. Hyperbolic cooling model

The permittivities and the permittivity products of bulk hBN and WSe_2 have been calculated through density functional perturbation theory, as implemented in the *abinit* code,[1] and the computational setup of Ref.[2] Along the trigonal axis zz, and, in-plane directions xx and yy, two bands of hyperbolicity can be observed in the low energy limit (energy less than 200 meV) due to hyperbolic optical phonons. The energy bands of hyperbolicity are strongly reduced in WSe_2 as compared to hBN, see Fig. S1b.

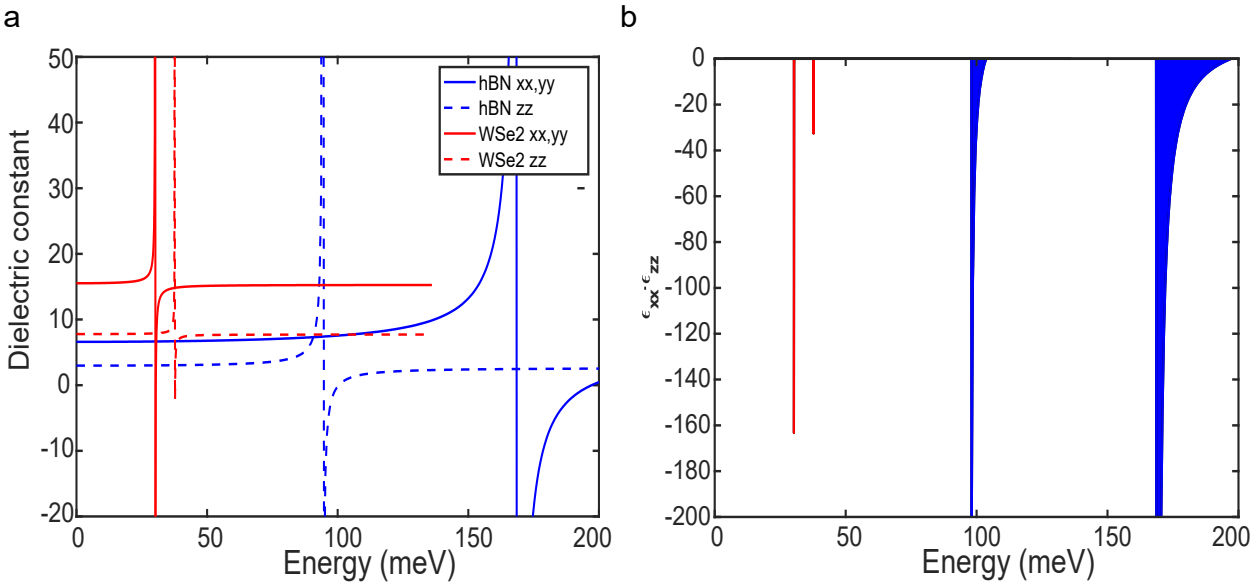

Figure S1: **Hyperbolic phonons in hBN and WSe_2. a)** Calculated dielectric constants of hBN (blue lines) and WSe_2 (red lines) along the in plane directions (xx and yy, solid lines) and along the c-axis (zz, dashed lines). **b)** Hyperbolic bands in hBN (blue curves and areas) and WSe_2 (red lines and areas) corresponding to energy ranges of panel a in which the dielectric constants along the in-plane (ϵ_{xx}) and out-of-plane (ϵ_{zz}) directions have opposite sign.

The electron cooling time calculated from the dielectric constants dispersion in Fig. S1 using the hyperbolic cooling theory[3–5] is reported in Fig. S2. The theory only considers the near-field coupling of the hot charge carriers of graphene with the hyperbolic phonons of WSe_2 as relaxation mechanism. Due to the reduced hyperbolicity, the cooling to hy-

perbolic phonons, which dominates in high-quality hBN-encapsulated single-layer graphene (SLG), is much less efficient in WSe_2-encapsulated SLG and the relaxation *via* emission of optical phonons eventually becomes the dominant process driving the cooling dynamics, in close analogy to suspended SLG. The expected cooling time *via* solely decay into hyperbolic phonons far exceeds, indeed, the few picoseconds recovery time measured by transient transmission in WSe_2-encapsulated graphene.

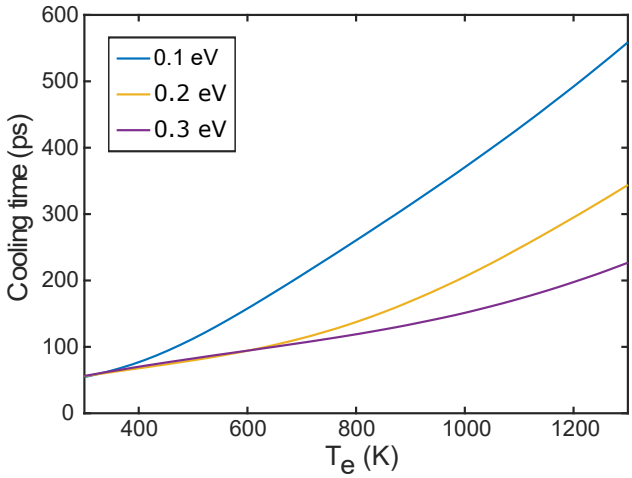

Figure S2: **Cooling time *via* near-field coupling with hyperbolic phonons of WSe_2.** Calculated hot electron cooling time considering the transfer of their excess-energy to the hyperbolic phonons of WSe_2 as a function of the initial electron temperature T_e, for three relevant values of the equilibrium chemical potential: 0.1, 0.2, 0.3 eV.

2. Cooling dynamics probed with terahertz pulses

The cooling dynamics of suspended graphene is measured by optical pump-THz probe (OPTP) ultrafast spectroscopy, to monitor the dynamics of intraband absorption following the photo-excitation, as sketched in Fig. S3. The spot size of the OPTP measurements is ~ 1 mm. Accordingly, we could use the same sample as used for TA measurements, with the probe illuminating both suspended and supported graphene, considering that the signal will be dominated by the suspended graphene.

In Fig. S4 a we show the OPTP dynamics for suspended graphene for a range of fluences. We note that we see much less of the fast decay component that is rather prominent in the TA

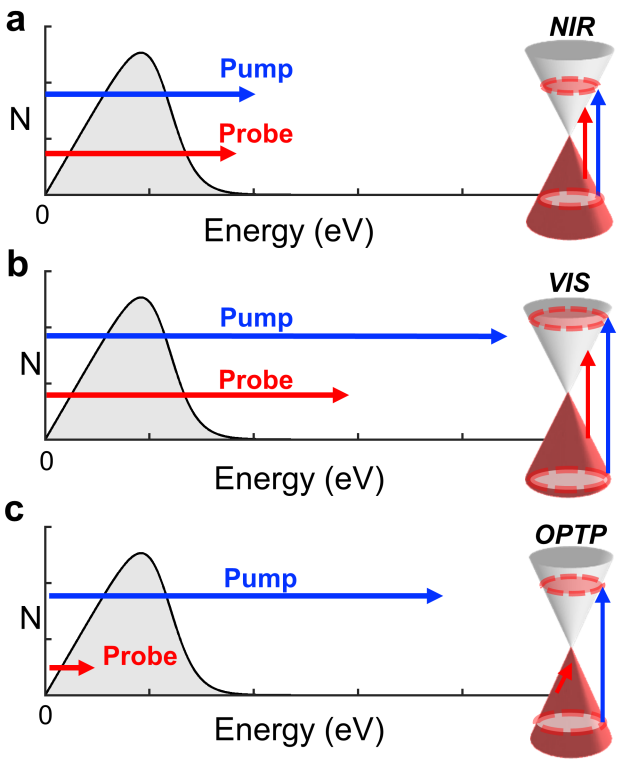

Figure S3: Schematic illustration of the carrier density as a function of carrier energy compared to the pump and probe photon energies of the three experimental configurations that we used: (a) near-infrared transient absorption (NIR), (b) visible transient absorption (VIS) and (c) optical-pump terahertz probe (OPTP). In all cases, the pump pulse is absorbed *via* interband transitions. For both TA configurations, the probe pulse is also associated with interband transitions, whereas the THz probe pulses are associated with the intraband conductivity. This is also clear in the accompanying Dirac cones with energy *vs.* momentum.

measurements. The reason for this is twofold. First of all, the superlinear relation between TA signal and ΔT_e makes the TA signal initially decay faster than the decay of the carrier temperature. Secondly, the time resolution of the OPTP measurement is ∼300 fs, compared to ∼100 fs for TA measurements, which broadens the initial fast decay.

With THz probe pulses, the transmission increases (for E_F >0.1 eV), as observed and explained in Refs.[7–9] and the change in transmission scales roughly linearly with the carrier temperature change ΔT_e, in contrast with the superlinear relation for TA measurements.

We compare the OPTP relaxation dynamics with the calculations based on the cooling mechanism involving high-energy (>0.16 eV) electrons cooling to optical phonons, which in turn cool to acoustic phonons, while the carrier system continuously re-thermalizes. We

describe these dynamics with the same model as before, using $E_F = 0.15$ eV and an optical phonon lifetime of 1.2 ps. Here, we have assumed a perfectly linear relation between OPTP signal and ΔT_e. We note that there is some underestimation of the signal magnitude for low fluences, and some overestimation for higher fluences, which shows that the assumption of linear scaling between signal and temperature change is a simplification, as it likely weakly sub-linear. However, the reasonable agreement between calculated and measured dynamics, confirms the validity of this intrinsic cooling mechanism. The slightly shorter optical phonon lifetime we extract by comparing the experimental data with our cooling model, is likely the result of the assumption of linear scaling between OPTP signal and ΔT_e

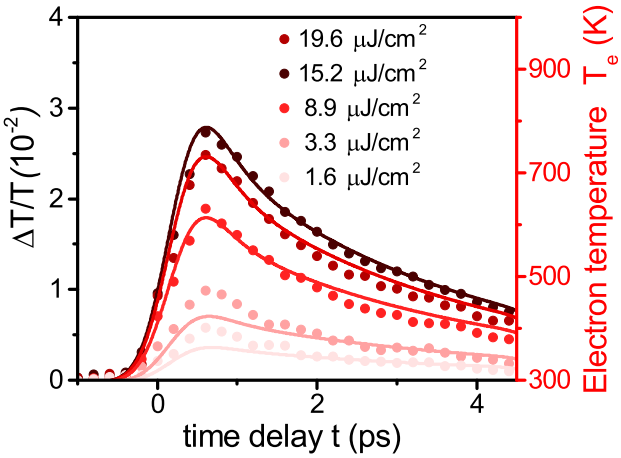

Figure S4: **Cooling dynamics of suspended graphene using THz pulses.** OPTP dynamics for high-quality suspended graphene with pump photon energy of 1.55 eV (800 nm) and probe photon energy around 4 meV (300 μm) together with the calculated cooling dynamics for the electron temperature T_e (solid lines).

3. Topography of encapsulated graphene

The thickness of the WSe_2 encapsulating flakes is determined from the AFM image in Fig. S5 by analysing a line profile cut from the map, which includes the substrate, whose height is assumed as z= 0, and both the bottom and top WSe_2 layers. The bottom and top WSe_2 layers have a thickness of 63 nm and 61 nm respectively, as obtained from the total thickness

of the heterostructure z= 124 nm.

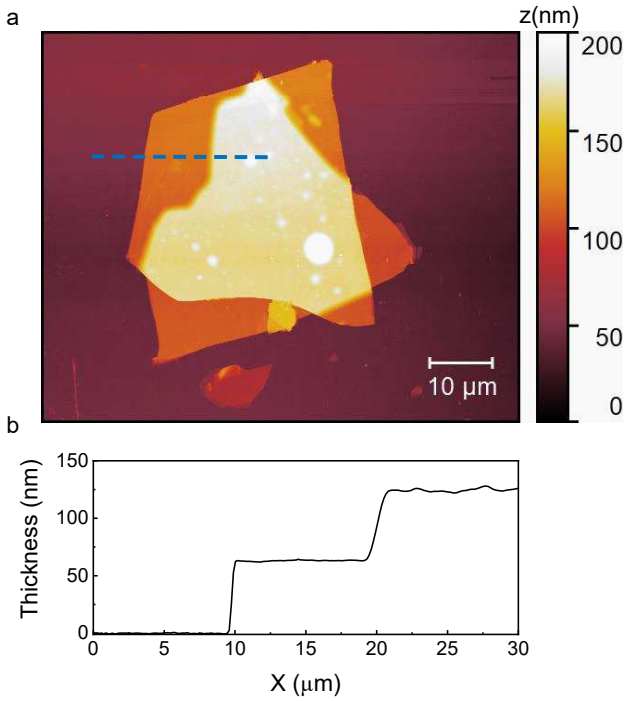

Figure S5: **Topography of WSe_2 encapsulated SLG. a)** AFM image of encapsulated SLG corresponding to Fig. 1 of the main text in a different color scale. **b)** Height profile extracted from the topography in panel a along the blue dashed line assuming the substrate level as zero.

4. Electron mobility of WSe_2-encapsulated graphene

The mobility of WSe_2 encapsulated graphene is determined by transport measurements reported in Fig. S6. A dual-gate field effect transistor based on encapsulated graphene is fabricated to monitor the resistance as a function of the charge carrier density n_e. The transistor channel has length L= 4.5 μm and width W= 4 μm. The top WSe_2 is 12 nm thick while the bottom layer is 34 nm. Efficient gating is achieved by stacking the heterostructure on top of an additional layer of hBN of thickness 25 nm. The resistance of graphene shows the typical ambipolar conduction with electron mobility $\mu_e \approx$ 39,000 $\mathrm{cm^2V^{-1}s^{-1}}$, and hole mobility $\mu_h \approx$ 36,000 $\mathrm{cm^2V^{-1}s^{-1}}$.

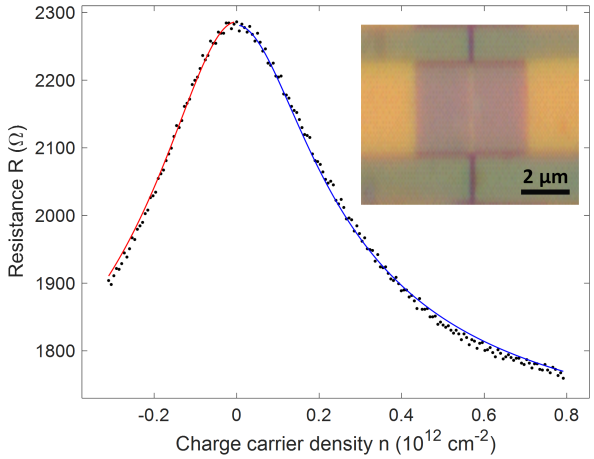

Figure S6: **Mobility of WSe_2 encapsulated graphene.** Charge transfer curve (black dots) for WSe_2 encapsulated graphene measured at room temperature applying 1 mV voltage bias to source-drain contacts of a dual-gate field effect transistor together with the best fit function for p-doping corresponding to hole mobility μ_h= 36,000 $\mathrm{cm^2V^{-1}s^{-1}}$ (red solid line), and, n-doping giving electron mobility μ_e= 39,000 $\mathrm{cm^2V^{-1}s^{-1}}$ (blue solid line). See inset for AFM image of the device.

5. Raman characterization of WSe_2-encapsulated graphene

The encapsulated SLG exhibits the vibrational fingerprints of bulk WSe_2 in the low frequency range, see Fig. S7a, corresponding to E_{1g} and E_{2g} modes.[10] The encapsulated SLG under 473 nm laser excitation exhibits photoluminescence signal in Fig. S7b with a peak at 776 nm due to the radiative recombination of the A exciton of bulk WSe_2 and one more intense peak at 908 nm attributable to the CaF_2 substrate.

Despite the intense luminescence background, the vibrational fingerprints of graphene can be identified in the encapsulated graphene. One exemplary spectrum acquired on fully encapsulated graphene with a 473 nm laser is reported in Fig. S8a, showing the 2D and G peaks. The 2D peak is fit with pseudoVoigt function centered at ω_{2D}= 2714.5 cm^{-1} with width Γ_{2D}= 25.7 cm^{-1}.

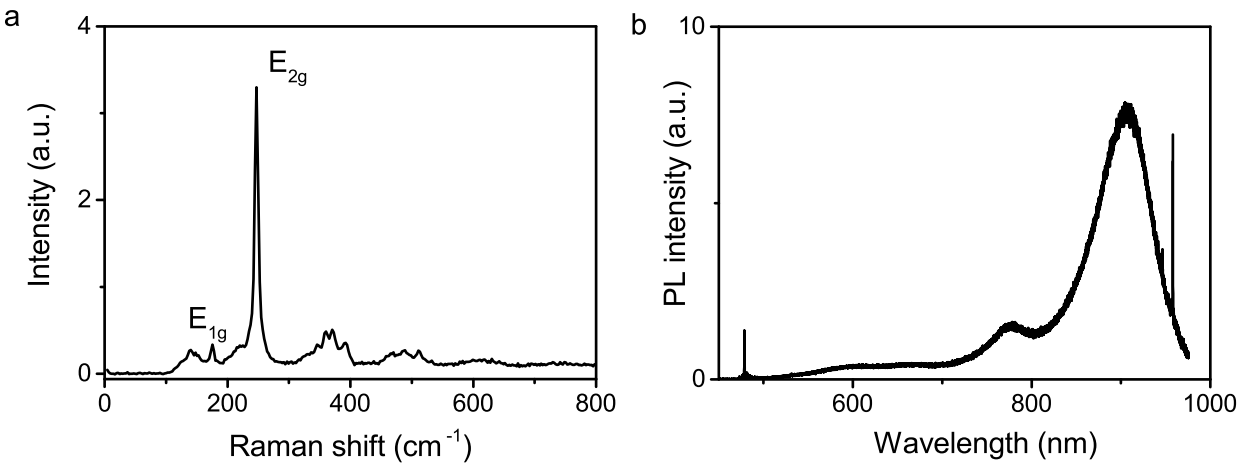

Figure S7: **Raman characterization of encapsulated SLG. a)** Raman spectroscopy measurements of the encapsulated SLG revealing the low-energy vibrational fingerprints of bulk WSe_2.[10] **b)** Photoluminescence (PL) of encapsulated SLG under 473 nm laser photoexcitation.

The substrate exhibits a Raman peak at around 1550 cm^{-1}, which has maximum amplitude outside the heterostructure. Accordingly, to retrieve the position and the width of the G peak, we analyse the peak at 1550 cm^{-1} as the sum of the peak from the substrate and of the G-peak, both described by pseudoVoigt functions. The retrieved energy position and

width of the G peak are equal to ω_G= 1585.2 cm^{-1} and Γ_G= 24.2 cm^{-1}.

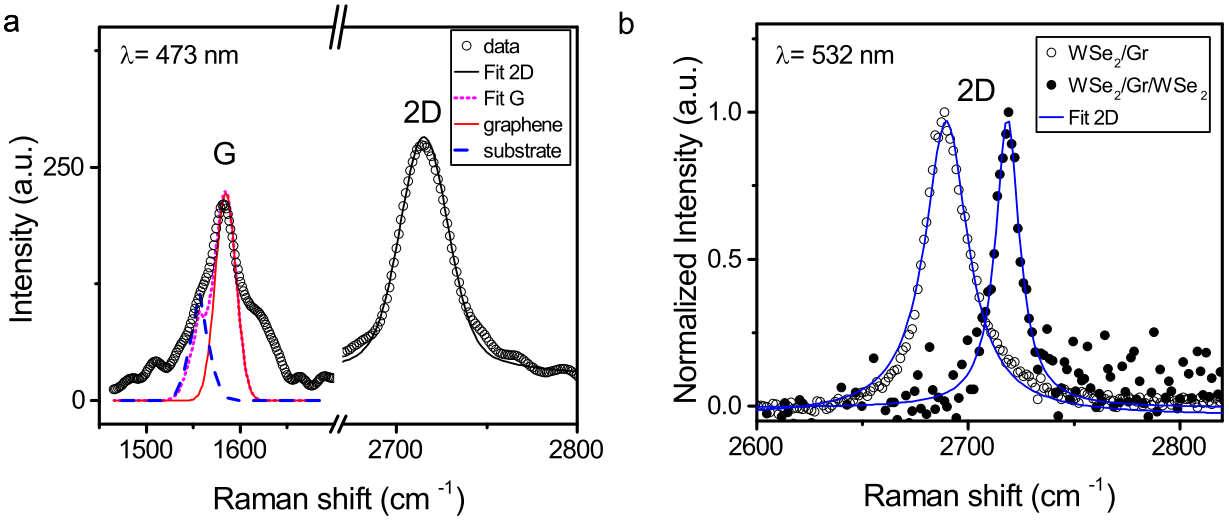

Figure S8: **Raman spectrum of WSe_2-encapsulated graphene and WSe_2-supported graphene. a)** Raman spectrum of WSe_2/Gr/WSe_2 acquired with 473 nm laser source (black dots). The 2D peaks is analysed with PseudoVoigt functions centered at ω_{2D} with width Γ_{2D} (black solid line). The peak at around 1550 cm^{-1} is analysed as the sum (magenta dotted line) of two peaks: one from the substrate, centered at about 1556 cm^{-1} (blue dashed line) and the G-peak of graphene (red line). **b)** Comparison of the 2D peak of encapsulated (WSe_2/Gr/WSe_2, full black dots) and uncovered graphene (WSe2/Gr, open black dots) acquired with 532 nm laser source and analysed with PseudoVoigt functions (blue solid lines).

6. Fully-encapsulated *vs.* semi-encapsulated graphene

In Fig. S8b we compare the 2D peak measured with a 532 nm laser source on fully encapsulated and uncovered graphene (semi-encapsulated). The 2D peak appears red-shifted and broader in sample regions where there is only the bottom WSe_2 flake and graphene is uncovered. In order to present the data in a clearer way, we have normalized the intensities of the 2D peaks in Fig. S8b. However, we report that the intensity ratio between the 2D peak on semi-encapsulated and fully-encapsulated region is ∼2.8. The best fit for the 2D peak in the two cases is obtained with a Pseudo Voigt function centered at ω_{2D}(WSe_2/Gr/WSe_2)= 2718 ± 1 cm^{-1} for the fully encapsulated and at ω_{2D}(WSe_2/Gr)= 2689 ± 0.2 cm^{-1} for the uncovered graphene. The extracted peak widths are Γ_{2D}(WSe_2/Gr/WSe_2)= 14 ± 2 cm^{-1}

for the fully-encapsulated and $\Gamma_{2D}(WSe_2/Gr) = 24.9 \pm 0.4$ cm^{-1} for the uncovered graphene. A blue-shift of ω_{2D} has been already observed with hBN encapsulation and be ascribed to the dielectric screening of e-ph interactions.[11] Moreover, the sharper 2D peak can indicate a more homogeneous strain distribution in the fully encapsulated regions that can come along with improved mobility.

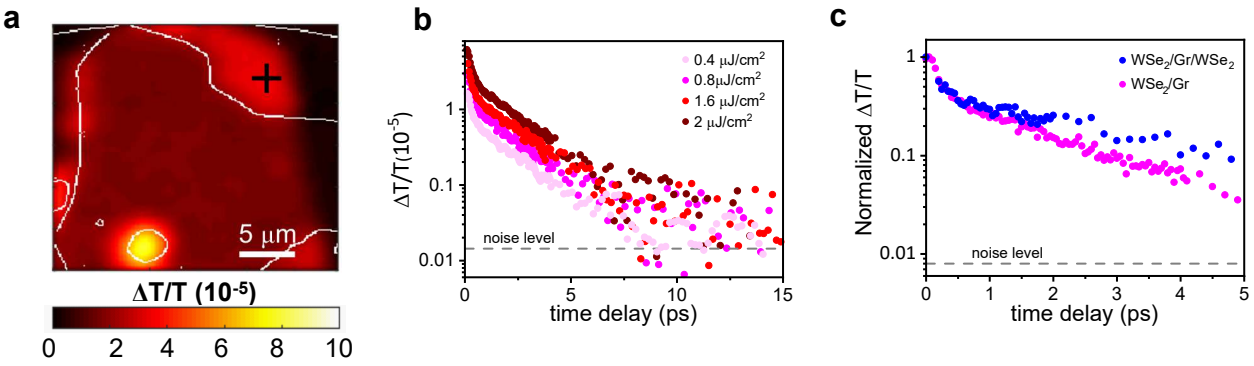

Figure S9: **Cooling dynamics of WSe_2-supported graphene.** Transient transmission $\Delta T/T$ maps of the WSe_2-encapsulated graphene at a fixed time delay t = 100 fs between pump and probe pulses acquired with pump at 0.8 eV (1550 nm) and probe at 0.729 eV (1700 nm). The black cross indicates the location in the WSe_2-supported graphene, where the $\Delta T/T$ dynamics reported in panel b are measured. b) $\Delta T/T$ dynamics measured on uncovered graphene with excitation fluences ranging from 0.4 to 2 μJ cm^{-2}. c) Comparison of normalized $\Delta T/T$ dynamics measured on fully-encapsulated (blue dots) and uncovered (red dots) graphene using a pump fluence of ~ 1 μJ cm^{-2}.

7. Differential reflectance of WSe_2-encapsulated graphene

The reflectance of the WSe_2 encapsulated graphene in the visible and near-infrared range is reported in Fig. S10. The absorption dips for photon energy 1.9 and 1.5 eV, are due to the excitations of bulk excitons of WSe_2: A at lower and B at higher energy.

The reflectance in the near-infrared region, far from the tail of the A-exciton, is completely attributable to graphene such that no difference is observed between the half (WSe_2/Gr) and the full (WSe_2/Gr/WSe_2) encapsulated sample. The pump and probe photons used in the transient transmission experiment are tuned at even lower photon energies, where only graphene is supposed to absorb.

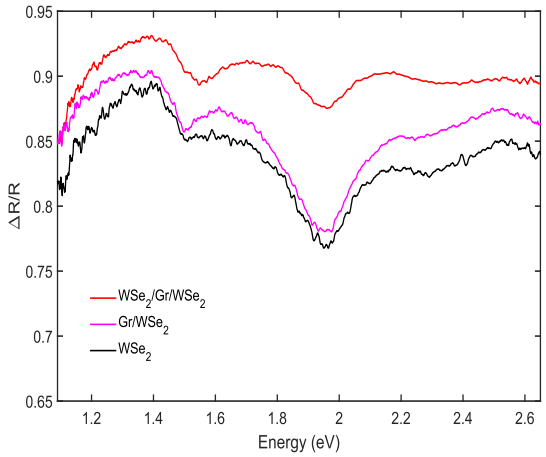

Figure S10: **Static reflectance of WSe_2-encapsulated graphene.** The static reflectance $\Delta R/R = \frac{R-R_0}{R_0}$ is evaluated by comparing the reflectance of the substrate R_0 with the reflectance R of the heterostructure. We compare the response at the WSe_2 bottom layer (black line), with that of fully WSe_2-encapsulated graphene (WSe_2/Gr/WSe_2, red-line) and with half-encapsulated graphene (Gr/WSe_2, magenta line).

8. Cooling due to lateral heat diffusion

The lateral diffusion of the heat transferred by the pump-pulse that is used to photo-excite graphene, can lead, under focused illumination, to a decay of the hot-electron temperature T_e and of the transient transmission signal. In-plane electronic heat conduction becomes particularly relevant for experiments using tight focusing over sub-micron spots and for high-mobility samples, since their large conductivity σ corresponds to large heat conductivity k_e, according to the Wiedemann-Franz law.

In order to estimate the impact of heat diffusion on the transient optical response of the high-mobility graphenes that we have studied, we model this decay, independent of other decay mechanisms, considering the spatial evolution of the Gaussian heat spot induced by the pump pulse, and the influence of the Gaussian spatial profile of probe beam.

The pump pulse intensity $I_{pump}(\mathbf{x})$ is modeled by 2D Gaussian spatial profile centered at

$\mathbf{x} = (x, y) = (0, 0)$:

$$I_{pump}(\mathbf{x}) = A_{pump} \exp\left(\frac{-|\mathbf{x}|^2}{2\sigma_{pump}^2}\right) =: G(A_{pump}, \sigma_{pump}). \tag{1}$$

where A_{pump} is the pump peak-intensity, and $2\sqrt{2ln(2)}\sigma_{pump}$ is its full-width-half-maximum (FWHM) that quantifies the spot size.

Within the pump/probe pulse duration, *i.e.* within less than 100 fs, an electron temperature profile $T_e(\mathbf{x}, t \approx 0) \propto I_{pump}(\mathbf{x})$ is induced in the photo-excited region of graphene. We assume it evolves isotropically in 2D with a constant electronic thermal diffusivity D following the heat equation:[12]

$$\frac{\partial}{\partial t} T_e = D \nabla^2 T_e. \tag{2}$$

The spatio-temporal evolution of this temperature profile $T_e(\mathbf{x}, t)$ is found by spatial convolution of the initial pump profile $I_{pump}(\mathbf{x})$ with the fundamental solution $\Phi(\mathbf{x}, t)$ of the heat equation,[12]

$$\Phi(\mathbf{x}, t) = \frac{1}{4\pi D t} \exp\left(-\frac{|\mathbf{x}|^2}{4Dt}\right), \tag{3}$$

leading to the following temperature profile decay:

$$\begin{aligned} T_e(\mathbf{x}, t) &\propto \int_{\mathbb{R}^2} \Phi(\mathbf{x} - \mathbf{y}, t) I_{pump}(\mathbf{y}) \\ &= \frac{A_{pump}}{1 + \frac{2Dt}{\sigma_{pump}^2}} \exp\left(\frac{-|\mathbf{x}|^2}{2(\sigma_{pump}^2 + 2Dt)}\right). \end{aligned} \tag{4}$$

In our experiments, the probe is focused onto a point detector, hence the temperature dynamics, eventually leading to the measured $\Delta T/T$ decay, is the result of an integration over the entire interaction region sampled by the probe.

In order to estimate the influence of the spatial profile of the probe beam intensity I_{pr}, we model it too as a Gaussian centered at $\mathbf{x} = 0$, $I_{pr}(\mathbf{x}) = G(A_{pr}, \sigma_{pr})$, such that the resulting

probed temperature dynamics are given by:

$$T_{\mathrm{e,probed}}(t) \propto \int_{\mathbb{R}^2} T_e(\mathbf{x},t)\cdot I_{pr}(\mathbf{x}) \\ = 2\pi A_{pump}A_{pr}\frac{\sigma_{pump}^2\sigma_{pr}^2}{\sigma_{pump}^2+\sigma_{pr}^2+2Dt}. \tag{5}$$

which shows that this decay mechanism becomes faster for decreasing pump and probe spot sizes(σ_{pump}, σ_{pr}) and for systems with large D.

We calculate the probed electron temperature dynamics expected in our experimental conditions for in-plane lateral heat diffusion using Eq. 5.

For graphene, the electronic heat diffusivity D is related to the electron mobility μ, and the Fermi energy E_F *via* the Einstein relation:[13] D = $\frac{E_F}{2e}\mu$, where e is the elementary charge.

For the NIR TA measurements of WSe_2-encapsulated graphene (Fig. 2 in the main text), we assume E_F =0.1 eV (which is an upper limit) and μ= 37,500 cm^2/Vs, leading to $D \approx$ 1875 cm^2/s.

For the VIS TA measurements of suspended graphene (Fig. 4 in the main text), the Fermi energy E_F= 0.18 eV and the mobility μ= 17,000 cm^2/Vs (which is an upper limit), leads to $D \approx$ 1530 cm^2/s.

For both measurements, the following pump and probe spot sizes are extracted by analyzing the maps of probe transmission T and transient transmission $\Delta T/T$ signal, acquired just before measuring the $\Delta T/T$ dynamics, see Fig. S11:
$\mathrm{FWHM}_{\mathrm{pump}}^{\mathrm{NIR}} = (3.01 \pm 0.23)\ \mu$m, $\mathrm{FWHM}_{\mathrm{probe}}^{\mathrm{NIR}} = (2.80 \pm 0.15)\ \mu$m,
$\mathrm{FWHM}_{\mathrm{pump}}^{\mathrm{VIS}} = (1.35 \pm 0.45)\ \mu$m, $\mathrm{FWHM}_{\mathrm{probe}}^{\mathrm{VIS}} = (0.91 \pm 0.15)\ \mu$m.

Figures S12a-b show the calculated decays for the two experiments compared to the highest fluence (slowest) experimental dynamics. In both the cases, the experimental decay is faster than what expected for lateral heat diffusion. The relaxation through emission of optical phonons, which is an intrinsic mechanism, independent on the specific size of

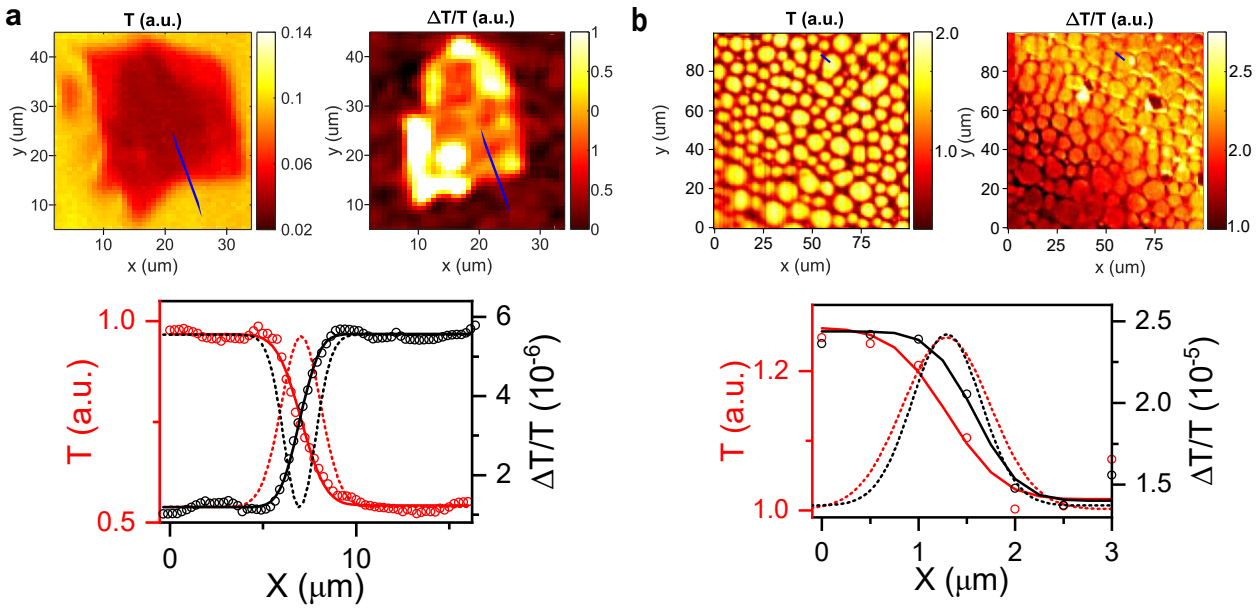

Figure S11: **a-b)** Line-profiles extracted from transmission T (red open dots) and transient transmission $\Delta T/T$ (black open dots) maps measured on WSe_2/Gr/WSe_2 (a) and suspended graphene (b) corresponding to the cut sketched by the blue lines on the maps. Data (open dots) are shown together with the best fit functions (black and red solid lines) defined by a Heaviside function, describing the step-like variation of T and $\Delta T/T$, convoluted with a Gaussian (dot lines) of full-width half maximum $\mathrm{FWHM_{probe}}$ (for T, red dot line) or $\mathrm{FWHM_{\Delta}}$ (for $\Delta T/T$, black dot line) that accounts for the finite spot size of pump and probe. The pump spot size $\mathrm{FWHM_{pump}}$ is extracted from the relation $(\mathrm{FWHM_{pump}})^{-2} = (\mathrm{FWHM_{\Delta}})^{-2} - (\mathrm{FWHM_{probe}})^{-2}$, that follows from the linear proportion of $\Delta T/T$ to the product of pump and probe intensities.

the beam used to monitor the optical properties of graphene, appears faster than in-plane electronic heat conduction even in the experiment on suspended graphene where the size of the holes imposed smaller spots.

Furthermore, according to Eq. 5, for increasing pump fluences, we would expect a faster cooling through heat diffusion, because higher electron temperature leads to a higher diffusivity D.[13] The fact that we observe an opposite trend in our experiments (Figure 2 and 4 of the main), indicates that the lateral heat diffusion is not dominating the hot-electron relaxation.

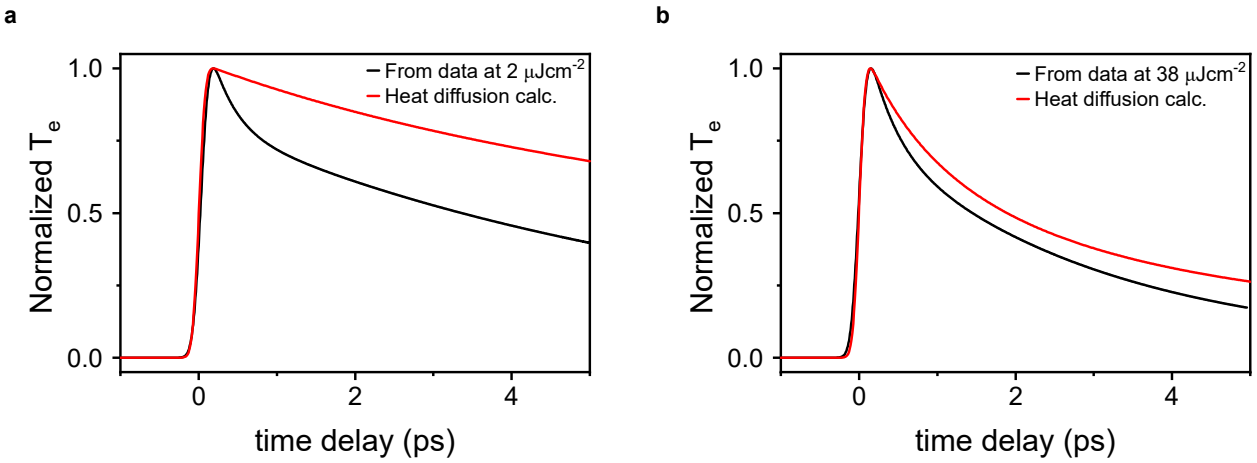

Figure S12: **Calculated decays due to lateral heat diffusion** a-b) Calculated hot-electron temperature dynamics for lateral heat diffusion according to Eq. 5, compared to the highest fluence experimental dynamics retrieved on the WSe_2/Gr/WSe_2 (a) and on suspended graphene in the VIS (b), using the experimental values of pump and probe spot sizes from Fig. S11.

9. Cooling *via* disorder-assisted acoustic phonon scattering

We calculate the cooling time through disorder-assisted scattering with acoustic phonons following Ref.,[14] which was based on Ref.[15] For this calculation, we assume that the electrical mobility is limited by disorder scattering, although there is actually a large contribution from long-range Coulomb scattering. This type of scattering does not contribute to disorder-assisted cooling, which means that by assuming a disorder-dominated electrical mobility we obtain a lower bound for the cooling time. We calculate the cooling time using $\tau_{\rm cool}^{\rm SC} = (3\frac{A}{\alpha} \cdot T_{\rm l})^{-1}$, where $T_{\rm l}$ is the lattice temperature (300 K), and $\frac{A}{\alpha} = \frac{2\ \lambda\ k_{\rm B}}{3\ k_{\rm F}\ \ell\ \hbar}$. Here, $k_{\rm B}$ is Boltzmann's constant, Fermi momentum $k_{\rm F} = \frac{E_{\rm F}}{\hbar\ v_{\rm F}}$, with $v_{\rm F}$ the Fermi velocity, and the mean free path is $\ell = v_{\rm F}\ \tau_{\rm ms}$, where the momentum scattering time is given by $\tau_{\rm ms} = \frac{\mu\ E_{\rm F}}{e\ v_{\rm F}^2}$. Finally, $\lambda = \frac{D^2\ 2\ E_{\rm F}}{\rho\ v_{\rm s}^2\ \pi\ (\hbar\ v_{\rm F})^2}$, where ρ is the mass density and $v_{\rm s}$ is the sound velocity. For the deformation potential D we chose 15 eV. With these equations, we obtain a cooling time $\tau_{\rm cool}^{\rm SC} = 22$ ps for WSe_2-encapsulated graphene with $\mu \approx$50,000 cm^{2}V^{-1}s^{-1} and $E_{\rm F} \approx$0.1 eV. For suspended graphene with $\mu \approx$17,000 cm^{2}V^{-1}s^{-1} and $E_{\rm F} \approx$0.18 eV, we find $\tau_{\rm cool}^{\rm SC} =$ 14 ps. Given these timescales, and the fact that they are lower bounds, we conclude that

disorder-assisted cooling does not play an important role in our samples.

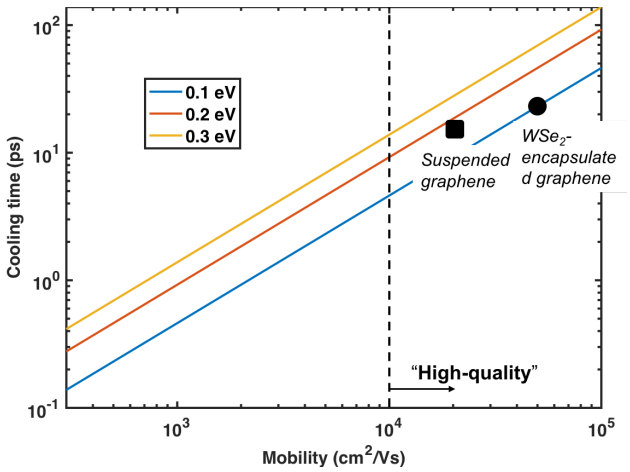

Figure S13: **Calculated "supercollision" cooling times**

10. Cooling *via* optical phonons

The cooling of electrons to optical phonons is described by means of the following rate equations for the electronic and optical-phonon temperatures, $T_e(t)$ and $T_\alpha(t)$, respectively:

$$\begin{cases} C_e\big(T_e(t)\big)\partial_t T_e(t) = -\hbar\sum_\alpha \omega_\alpha \mathcal{R}_\alpha\big(T_e(t), T_\alpha(t)\big) \\ \mathcal{D}\big(\omega_\alpha, T_\alpha(t)\big)\partial_t T_\alpha(t) = \dfrac{\mathcal{R}_\alpha\big(T_e(t), T_\alpha(t)\big)}{M_\alpha\big(T_e(t)\big)} - \gamma_\alpha\big[n_\alpha\big(T_\alpha(t)\big) - n_\alpha(T_\alpha^{(0)})\big] \end{cases}, \tag{6}$$

where $C_e(T_e)$ is the electron heat capacity, the sum is over phonon modes (labelled by α), ω_α is the frequency of mode α, and $\mathcal{R}_\alpha(T_e, T_\alpha)$ is the rate of α-phonon emission. Its expression is derived in the following section from a microscopic Boltzmann-equation approach [see Eq. (20)]. Furthermore, $\mathcal{D}(\omega_\alpha, T_\alpha) = \partial n_\alpha(T_\alpha)/(\partial T_\alpha)$, where $n_\alpha(T_\alpha) = [e^{\hbar\omega_\alpha/(k_B T_\alpha)} - 1]^{-1}$ is the phonon occupation function, while $T_\alpha^{(0)}$ is the equilibrium phonon temperature (in our calculations, the lattice temperature T_L) and γ_α is a phenomenological damping rate encoding, *e.g.*, the decay of optical phonons into acoustic ones. In our calculation we consider phonon modes at the Γ and K/K' points of the phonon Brillouin zone, which scatter electrons in the same valley or between different valleys, respectively. Finally ($v_F \simeq 10^6$ m/s is the

electron Fermi velocity),

$$M_\alpha(T_e) = \frac{N_\alpha}{4\pi}\left[\left(\frac{\varepsilon_{\max}(T_e)}{\hbar v_{\rm F}}\right)^2 - \left(\frac{\varepsilon_{\min}(T_e)}{\hbar v_{\rm F}}\right)^2\right], \tag{7}$$

is the phonon density of states. $M_\alpha(T_e)$ measures the size of the portion (an annulus) of phonon Brillouin zone that is heated in the electron-cooling process and depends, assuming the phonon dispersion to be flat, on the maximum momentum that can be exchanged between electrons and phonons. As such, $M_\alpha(T_e)$ depends on the electron temperature. In Eq. (7), N_α is the phonon degeneracy ($N_\alpha = 2$ for both Γ- and K-phonons – see below), while $\varepsilon_{\min}(T_e)$ and $\varepsilon_{\max}(T_e)$ are the minimum and maximum phonon energies, respectively. Their expressions are derived in the following.

The time-evolution of electronic temperature dynamics is converted into the dynamics of the differential conductance *via*[16,17]

$$\frac{\Delta T}{T}(t) = -\frac{4\pi}{c}\frac{2}{n_1+n_2}\Delta\sigma\big(\omega_{\rm ph}, T_e(t)\big)\ , \tag{8}$$

where n_1 and n_2 are the refractive indices of the media above and below the graphene sheet, $\hbar\omega_{\rm ph}$ is the photon excitation energy, $\Delta\sigma(\omega_{\rm ph}, T_e) = \sigma(\omega_{\rm ph}, T_e) - \sigma(\omega_{\rm ph}, T_L)$ and

$$\sigma(\omega_{\rm ph}, T_e) = \frac{e^2}{4\hbar}\left[f(\frac{-\hbar\omega_{\rm ph}/2-\mu}{k_{\rm B}T_e}) - f(\frac{\hbar\omega_{\rm ph}/2-\mu}{k_{\rm B}T_e})\right]\ , \tag{9}$$

is the electronic optical conductivity. Here, $f(x) = (e^x+1)^{-1}$ if the Fermi-Dirac distribution function, while μ is the time-dependent electron chemical potential (see below).

Microscopic derivation of the electron-phonon cooling rate

We start from the Boltzmann equation satisfied by the electron distribution function, $f_{\boldsymbol{k},\lambda}$ (momentum $\boldsymbol{k}$, band $\lambda = \pm$), in a homogeneous system and in the absence of forces:

$$\partial_t f_{\boldsymbol{k},\lambda} = \sum_\alpha \mathcal{I}_{\boldsymbol{k},\lambda,\alpha} \ . \tag{10}$$

The right-hand side of this equation is the sum of collision integrals accounting for the scattering between electrons and given phonon modes:

$$\mathcal{I}_{\boldsymbol{k},\lambda,\alpha} = \sum_{\boldsymbol{k}',\lambda'} \left[f_{\boldsymbol{k},\lambda}(1 - f_{\boldsymbol{k}',\lambda'}) W^{(\alpha)}_{\boldsymbol{k},\lambda\to\boldsymbol{k}',\lambda'} - f_{\boldsymbol{k}',\lambda'}(1 - f_{\boldsymbol{k},\lambda}) W^{(\alpha)}_{\boldsymbol{k}',\lambda'\to\boldsymbol{k},\lambda} \right] \ , \tag{11}$$

where the transition probability, within a Fermi-golden rule approach, is

$$\begin{aligned} W^{(\alpha)}_{\boldsymbol{k},\lambda\to\boldsymbol{k}',\lambda'} &= \frac{2\pi}{\hbar V} \sum_{\boldsymbol{q},\nu} \left| U_{\lambda,\lambda',\alpha}(\boldsymbol{k},\boldsymbol{k}',\boldsymbol{q}) \right|^2 \big[(n_{\boldsymbol{q},\alpha} + 1) \delta(\varepsilon_{\boldsymbol{k},\lambda} - \varepsilon_{\boldsymbol{k}',\lambda'} - \hbar\omega_{\boldsymbol{q},\alpha}) \delta(\boldsymbol{k} - \boldsymbol{k}' - \boldsymbol{q}) \\ &+ n_{\boldsymbol{q},\alpha} \delta(\varepsilon_{\boldsymbol{k},\lambda} - \varepsilon_{\boldsymbol{k}',\lambda'} + \hbar\omega_{\boldsymbol{q},\alpha}) \delta(\boldsymbol{k} - \boldsymbol{k}' + \boldsymbol{q}) \big] \ . \end{aligned} \tag{12}$$

Here $\varepsilon_{\boldsymbol{k},\lambda}$ is the electron band energy, $n_{\boldsymbol{q},\alpha}$ is the non-equilibrium photon distribution functions and $U_{\lambda,\lambda',\alpha}(\boldsymbol{k},\boldsymbol{k}',\boldsymbol{q})$ is the electron-phonon interaction. There are two degenerate optical-phonon modes at the Γ point, longitudinal and transverse, both with energy $\hbar\omega_\Gamma = 196$ meV, which induce intra-valley electronic transitions. For these,[18]

$$\left| U_{\lambda,\lambda',\Gamma}(\boldsymbol{k},\boldsymbol{k}',\boldsymbol{q}) \right|^2 = g_\Gamma^2 \left[1 \pm \lambda\lambda' \cos\left(\varphi_{\boldsymbol{k}} + \varphi_{\boldsymbol{k}'} - 2\varphi_{\boldsymbol{q}} \right) \right] \ , \tag{13}$$

where the plus (minus) sign applies to longitudinal (transverse) phonons. We will assume that these modes are equally populated, *i.e.* their temperatures are equal to $T_\Gamma(t)$. In what follows, we will add up their contributions to the heat dissipated into a singe function $\mathcal{Q}_\Gamma(T_e, T_\Gamma)$.

Similarly, the modes at the K and K' points of the phonon Brillouin zone are degenerate

with energy $\hbar\omega_K = 161$ meV and, under the assumption that they are equally populated at the temperature $T_K(t)$, their contributions will be considered together with a singe function $\mathcal{Q}_K(T_e, T_K)$. These phonon induce inter-valley electronic transitions: the K-point phonons scatter electrons from valley K to K', while the K'-phonons scatter them in the opposite way. For these phonons,[18]

$$\left|U_{\lambda,\lambda',K/K'}(\boldsymbol{k},\boldsymbol{k}',\boldsymbol{q})\right|^2 = g_K^2\left[1 \mp \lambda\lambda'\cos(\varphi_{\boldsymbol{k}} - \varphi_{\boldsymbol{k}'})\right] . \tag{14}$$

In these equations,

$$g_\alpha = \beta_\alpha\sqrt{\frac{\hbar}{2\rho_m\omega_\alpha}} , \tag{15}$$

where[18] the graphene mass density is $\rho_m = 7.6 \times 10^{-7}$ kg/m^2. We note that $\beta_K^2 = 2\beta_\Gamma^2$, and that the latter can be rewritten as[18]

$$\beta_\Gamma = \frac{3}{2}\frac{\partial t}{\partial a} , \tag{16}$$

where t is the nearest-neighbor hopping amplitude and a the carbon-carbon distance. The parameter β_Γ has been calculated by DFT, GW and also estimated experimentally.[18] Its value varies quite substantially depending on the source. To be conservative, we will use $\beta_\Gamma = 11.4$ eV/Å[18] as taken from the GW level of *ab initio* simulations, to be consistent with the chosen Fermi velocity of $v_\mathrm{F} = 10^6$ m/s. For later use, we define

$$\tilde{g}_\alpha = \beta_\Gamma\sqrt{\frac{\hbar}{2\rho_m\omega_\alpha}} . \tag{17}$$

Multiplying Eq. (10) by the energy measured from the chemical potential $\mu \equiv \mu(T_e)$, $\varepsilon_{\boldsymbol{k},\lambda} - \mu$, integrating it over momentum $\boldsymbol{k}$ and summing over the band λ, we get the equation

of motion for the electron energy, $\partial_t \mathcal{E}(T_e) = -\sum_\alpha \mathcal{Q}_\alpha(T_e, T_\alpha)$, where

$$\mathcal{Q}_\alpha(T_e, T_\alpha) = \hbar\omega_\alpha \frac{4\pi}{\hbar N_{\rm f}} \tilde{g}_\alpha^2 \left[n_\alpha(T_\alpha) - n_\alpha(T_e)\right] \left[\tilde{\mathcal{Q}}(\mu, \omega_\alpha) - \tilde{\mathcal{Q}}(\mu + \omega_\alpha, \omega_\alpha)\right] \ , \tag{18}$$

is the heat density dissipated in collisions with the phonons of mode α. Note that $\mathcal{Q}_\Gamma(T_e, T_K)$ contains the effect of both longitudinal and transverse phonons, while $\mathcal{Q}_K(T_e, T_K)$ accounts also for the contribution of modes at K'. In Eq. (18), $N_{\rm f} = 4$ is the spin-valley degeneracy of graphene, and

$$\tilde{\mathcal{Q}}(\mu, \omega) \ = \ \int_{-\infty}^{+\infty} d\varepsilon \ \nu(\varepsilon) \ \nu(\varepsilon - \omega) \left[f\left(\frac{\varepsilon - \mu}{k_{\rm B} T_e}\right) - \Theta(-\varepsilon) \right] \ . \tag{19}$$

In this equation, $\nu(|\varepsilon|) = N_{\rm f}|\varepsilon|/(2\pi\hbar^2 v_{\rm F}^2)$ is the Dirac-fermion density of states. Interestingly, $\mathcal{Q}_\Gamma$ and $\mathcal{Q}_K$ have the same functional dependence on the respective phonon frequencies and temperatures, *i.e.* all coefficients in the two definitions are the same. This is due to the fact that, while the phonons at Γ are doubly degenerate, the interaction vertex g_K^2 is twice g_Γ^2. From Eq. (18), using the fact that all phonons of a given mode α have the same frequency, it is possible to define the rate of phonon emission

$$\mathcal{R}_\alpha(T_e, T_\alpha) = \frac{\mathcal{Q}_\alpha(T_e, T_\alpha)}{\hbar\omega_\alpha} \ . \tag{20}$$

Introducing the (density of) electronic heat capacity

$$C_e(T_e) = \int_{-\infty}^{\infty} d\varepsilon \ \nu(|\varepsilon|)(\varepsilon - \mu) \left[-\frac{\partial f\left[(\varepsilon - \mu)/(k_{\rm B} T_e)\right]}{\partial \varepsilon} \right] \left[\frac{\varepsilon - \mu}{T_e} + \frac{\partial \mu}{\partial T_e} \right] \ , \tag{21}$$

we finally get

$$C_e(T_e) \partial_t T_{\rm e} = -\sum_\alpha \mathcal{Q}_\alpha(T_e, T_\alpha) \ , \tag{22}$$

from which it is possible to define the instantaneous electron-α-phonon cooling time τ_α

$$\tau_\alpha = \left[\frac{\mathcal{Q}_\alpha(T_e, T_\alpha)/C_e(T_e)}{T_e - T_\alpha}\right]^{-1} \quad . \tag{23}$$

In all equations, the chemical potential is determined by (numerically) inverting the equation

$$n = \frac{N_{\rm F}(k_{\rm B}T_e)^2}{2\pi(\hbar v_{\rm F})^2}\left[{\rm Li}_2(-e^{-\mu/(k_{\rm B}T_e)}) - {\rm Li}_2(-e^{\mu/(k_{\rm B}T_e)})\right] \ , \tag{24}$$

fixing the electronics density n. Here, ${\rm Li}_n(x)$ is the n-th polylogarithmic function. The derivative of the chemical potential is readily evaluated, under the assumption of a constant density, as

$$\frac{\partial\mu}{\partial T_e} = \frac{\mu}{T_e} - k_{\rm B}\frac{{\rm Li}_2(-e^{-\mu/(k_{\rm B}T_e)}) - {\rm Li}_2(-e^{\mu/(k_{\rm B}T_e)})}{\ln(1+e^{\mu/(k_{\rm B}T_e)}) + \ln(1+e^{-\mu/(k_{\rm B}T_e)})} \ . \tag{25}$$

We note that the integral in Eq. (21) can be carried out analytically to give

$$\begin{aligned} C_e(T_e) &= k_{\rm B}\frac{N_{\rm F}(k_{\rm B}T_e)^2}{2\pi(\hbar v_{\rm F})^2}\Big\{ \left[3\big(F_{+,2}(x) - F_{-,2}(x)\big) - 4x\big(F_{+,1}(x) - F_{-,1}(x)\big) + x^2\big(F_{+,0}(x) - F_{-,0}(x)\big)\right] \\ &+ \frac{\partial\mu}{\partial(k_{\rm B}T)}\left[2\big(F_{+,1}(x) - F_{-,1}(x)\big) - x\big(F_{+,0}(x) - F_{-,0}(x)\big)\right]\Big\}_{x=\mu/(k_{\rm B}T_e)} \ . \end{aligned} \tag{26}$$

Here we defined

$$\begin{aligned} F_{-,n}(x) &= \int_{-\infty}^{0} dy\ y^n\left[f\left(y-x\right) - \Theta(-y)\right] \ , \\ F_{+,n}(x) &= \int_{0}^{+\infty} dy\ y^n\left[f\left(y-x\right) - \Theta(-y)\right] \ . \end{aligned} \tag{27}$$

These integrals are calculated explicitly for the first few values of n to give

$$\begin{aligned} F_{\pm,0}(x) &= \pm \ln(1+e^{\pm x}) \ , \\ F_{\pm,1}(x) &= -\mathrm{Li}_2(-e^{\pm x}) \ , \\ F_{\pm,2}(x) &= \mp 2\mathrm{Li}_3(-e^{\pm x}) \ , \\ F_{\pm,3}(x) &= -6\mathrm{Li}_4(-e^{\pm x}) \ . \end{aligned} \tag{28}$$

Similarly, defining

$$\tilde{F}_n(x,w) = \int_0^w dy \ y^n \big[f\,(y-x) - \Theta(-y) \big] \ . \tag{29}$$

such that

$$\begin{aligned} \tilde{F}_0(x,w) &= \ln(1+e^x) - \ln(1+e^{x-w}) \ , \\ \tilde{F}_1(x,w) &= \mathrm{Li}_2(-e^{x-w}) - \mathrm{Li}_2(-e^x) - w\ln(1+e^{x-w}) \ , \\ \tilde{F}_2(x,w) &= 2\mathrm{Li}_3(-e^{x-w}) - 2\mathrm{Li}_3(-e^x) + 2w\mathrm{Li}_2(-e^{x-w}) - w^2\ln(1+e^{x-w}) \ , \end{aligned} \tag{30}$$

Eq. (19) can be integrated analytically to give

$$\begin{aligned} \tilde{\mathcal{Q}}(\mu,\omega) &= \left(\frac{N_\mathrm{F}}{2\pi(\hbar v_\mathrm{F})^2}\right)^2 (k_\mathrm{B}T_e)^3 \Big\{ \big[F_{+,2}(x) + F_{-,2}(x)\big] - w\big[F_{+,1}(x) + F_{+,1}(x)\big] \\ &- 2\big[\tilde{F}_2(x,w) - w\tilde{F}_1(x,w)\big] \Big\}_{x=\mu/(k_\mathrm{B}T_e), w=\omega/(k_\mathrm{BT_e})} \ . \end{aligned} \tag{31}$$

The phonon density of states

Given the temperatures and densities we are working at, the largest contribution to electron cooling comes from intraband processes. These must satisfy:

$$v_{\rm F}|\boldsymbol{k}+\boldsymbol{q}| = v_{\rm F}k - \omega \;\Rightarrow\; \begin{cases} 0 < \omega < v_{\rm F}k \\ q_{\pm}(\theta) = -k\cos(\theta) + \sqrt{k^2\cos^2(\theta) + \dfrac{\omega^2}{v_{\rm F}^2} - 2\dfrac{\omega}{v_{\rm F}}k} \end{cases} . \tag{32}$$

The maximum and minimum momenta of the phonon are

$$\begin{aligned} q_{\rm min} &= q_{-}(\pi) = \omega/v_{\rm F} \ , \\ q_{\rm max} &= q_{+}(\pi) = 2k - \omega/v_{\rm F} \ . \end{aligned} \tag{33}$$

The maximum and minimum values of k are determined by considering the difference of Fermi functions:

$$f\left(\frac{\varepsilon_{\boldsymbol{k},+}-\mu}{k_{\rm B}T}\right) - f\left(\frac{\varepsilon_{\boldsymbol{k},+}-\mu-\hbar\omega}{k_{\rm B}T}\right) \ . \tag{34}$$

The function $\mathcal{F}(x,y) = f(x-y) - f(x)$, where $x = (\varepsilon_{\boldsymbol{k},+}-\mu)/(k_{\rm B}T)$ and $y = \hbar\omega/(k_{\rm B}T)$ can be viewed as a distribution in x. Its mean value is approximately $y/2$, while its standard deviation is

$$\sigma(y) = \sqrt{\frac{4\pi^2+y^2}{12}} \ . \tag{35}$$

Therefore, the difference in Fermi functions implies that k is approximately bounded within

$$\mu + \frac{\hbar\omega}{2} - \nu k_{\rm B}T\sigma\left(\frac{\hbar\omega}{k_{\rm B}T}\right) \lesssim v_{\rm F}k \lesssim \mu + \frac{\hbar\omega}{2} + \nu k_{\rm B}T\sigma\left(\frac{\hbar\omega}{k_{\rm B}T}\right) \ , \tag{36}$$

where ν here is a fitting parameter of order one. Therefore,

$$\frac{\omega}{v_{\rm F}} \lesssim q \lesssim 2\left[\frac{\mu}{\hbar v_{\rm F}} + \nu\frac{k_{\rm B}T}{\hbar v_{\rm F}}\sigma\left(\frac{\hbar\omega}{k_{\rm B}T}\right)\right] \ . \tag{37}$$

To obtain this equation we substituted the maximum k of Eq. (36) into $q_{\max}$ of Eq. (33). We then get

$$\begin{cases} \varepsilon_{\min}(T_e) = \hbar\omega \\ \varepsilon_{\max}(T_e) = 2\left[\mu + \nu k_{\mathrm{B}} T \sigma\left(\dfrac{\hbar\omega}{k_{\mathrm{B}} T}\right)\right] \end{cases} . \tag{38}$$

References

1. Gonze, X.; Beuken, J.-M.; Caracas, R.; Detraux, F.; Fuchs, M.; Rignanese, G.-M.; Sindic, L.; Verstraete, M.; Zerah, G.; Jollet, F.; Torrent, M.; Roy, A.; Mikami, M.; Ghosez; Ph.; Raty, J.-Y.; Allan, D. C. First-Principles Computation of Material Properties: The ABINIT Software Project. *Comput. Mater. Sci.* **2002**, 25, 478–492

2. Pike, N. A.; Dewandre, A.; Van Troeye, B.; Gonze, X.; Verstraete, M. J. Vibrational and Dielectric Properties of the Bulk Transition Metal Dichalcogenides. *Phys. Rev. Mater.* **2018**, 2, 063608.

3. Principi, A.; Lundeberg, M. B.; Hesp, N. C.; Tielrooij, K. J.; Koppens, F. H.; Polini, M. Super-Planckian Electron Cooling in a van der Waals Stack. *Phys. Rev. Lett.* **2017**, 118, 1–6

4. Tielrooij, K.-J.; Hesp, N. C. H.; Principi, A.; Lundeberg, M. B.; Pogna, E. A. A.; Banszerus, L.; Mics, Z.; Massicotte, M.; Schmidt, P.; Davydovskaya, D.; Purdie, D. G.; Goykhman, I.; Soavi, G.; Lombardo, A.; Watanabe, K.; Taniguchi, T.; Bonn, M.; Turchinovich, D.; Stampfer, C.; Ferrari, A. C.; Cerullo, G.; Polini, M.; Koppens, F. H. L. Out-of-Plane Heat Transfer in van der Waals Stacks through Electron–Hyperbolic Phonon Coupling. *Nat. Nanotechnol.* **2018**, 13, 41–46

5. Yang, W.; Berthou, S.; Lu, X.; Wilmart, Q.; Denis, A.; Rosticher, M.; Taniguchi, T.; Watanabe, K.; Fève, G.; Berroir, J.-m.; Zhang, G.; Voisin, C.; Baudin, E.; Plaçais, B. A Graphene Zener-Klein Transistor Cooled by a Hyperbolic Substrate. *Nat. Nanotechnol.* **2018**, 13, 47–52

6. Robinson, J. A.; Wetherington, M.; Tedesco, J. L.; Campbell, P. M.; Weng, X.; Stitt, J.; Fanton, M. A.; Frantz, E.; Snyder, D.; VanMil, B. L.; Jernigan, G. G.; Rachael, L. M. W.; Eddy, C. R.; Gaskill, D. K. Correlating Raman Spectral Signatures with Carrier

Mobility in Epitaxial Graphene: A Guide to Achieving High Mobility on the Wafer Scale. *Nano Lett.* **2009**, 9, 2873–2876

7. Tielrooij, K.; Song, J.; Jensen, S. A.; Centeno, A.; Pesquera, A.; Elorza, A. Z.; Bonn, M.; Levitov, L.; Koppens, F. Photoexcitation Cascade and Multiple Hot-Carrier Generation in Graphene. *Nat. Phys.* **2013**, 9, 248–252

8. Frenzel, A. J.; Lui, C. H.; Shin, Y. C.; Kong, J.; Gedik, N.Semiconducting-to-Metallic Photoconductivity Crossover and Temperature-Dependent Drude Weight in Graphene. *Phys. Rev. Lett.* **2014**, 113, 56602

9. Tomadin, A.; Hornett, S. M.; Wang, H. I.; Alexeev, E. M.; Candini, A.; Coletti, C.; Turchinovich, D.; Kläui, M.; Bonn, M.; Koppens, F. H. L.; Hendry, E.; Polini, M.; Tielrooij, K.-J. The Ultrafast Dynamics and Conductivity of Photoexcited Graphene at Different Fermi Energies. *Sci. Adv.* **2018**, 4, eaar5313

10. Terrones, H.; Corro, E. D.; Feng, S.; Poumirol, J. M.; Rhodes, D.; Smirnov, D.; Pradhan, N. R.; Lin, Z. New First Order Raman-Active Modes in Few Layered Transition Metal. *Sci. Rep.* **2014**, 4, 4215

11. Forster, F.; Molina-Sanchez, A.; Engels, S.; Epping, A.; Watanabe, K.; Taniguchi, T.; Wirtz, L.; Stampfer, C. Dielectric Screening of the Kohn Anomaly of Graphene on Hexagonal Boron Nitride. *Phys. Rev. B* **2013**, 88, 085419

12. Crank, J., The Mathematics of Diffusion (Oxford University Press, Oxford, 1975)

13. Block, A.; Principi, A; Hesp, N. C. H.; Cummings, A. W.; Liebel, M.; Watanabe, K.; Taniguchi, T.; Roche, S.; Koppens, F. H. L.; van Hulst, N. F.; Tielrooij, K. J. Observation of Giant and Tuneable Thermal Diffusivity of Dirac Fluid at Room Temperature. **2020**, 2008.04189. arXiv. `http://arxiv.org/abs/2008.04189` (accessed 10 April 2021)

14. Graham, M. W.; Shi, S. F.; Ralph, D. C.; Park, J.; McEuen, P. L. Photocurrent Measurements of Supercollision Cooling in Graphene. *Nat. Phys.* **2013**, 9, 103–108

15. Song, J. C. W.; Reizer, M. Y.; Levitov, L. S. Disorder-Assisted Electron-Phonon Scattering and Cooling Pathways in Graphene. *Phys. Rev. Lett.* **2012**, 109, 106602

16. Stauber, T.; Peres, N.; Geim, A. Optical Conductivity of Graphene in the Visible Region of the Spectrum. *Phys. Rev. B* **2008**, 78, 085432

17. Falkovsky, L. Optical Properties of Graphene. *J. Phys.: Conf. Ser.* **2008**, 129, 012004

18. Sohier, T.; Calandra, M.; Park, C.-H.; Bonini, N.; Marzari, N.; Mauri, F. Phonon-Limited Resistivity of Graphene by First-Principles Calculations: Electron-Phonon-Interactions, Strain-Induced Gauge Field, and Boltzmann Equation. *Phys. Rev. B* **2014**, 90, 125414